Materials Advances

PAPER

Check for updates

Solid-state and aggregation-induced emission of novel bicyclic and tricyclic difluoroboron heterocycles†

Martina Žabenská,[a] Chiara Capolungo,[b] Chiara Mariani,[b] Damiano Genovese, [b] Tomáš Mikysek,[c] Jiří Váňa, [a] Aleš Růžička, [d] František Josefík,[a] Markéta Svobodová*[a] and Petr Šimůnek [*a]

Six novel bicyclic and tricyclic difluoroboron NBN and OBN heterocycles were designed here in the quest for novel luminogenic molecular architectures because of their strong application potential as active layers in optoelectronics and as responsive units in sensing. They were prepared and then characterized with spectral (UV-vis, NMR, and luminescence) and electrochemical methods, and assessed *via* theoretical and X-ray investigations. Most of the compounds are non-emissive in solution, but luminescent in the solid state (red or yellow-green luminescence), and they are AIE active, offering excellent contrast for sensing schemes. Keeping this in view, two compounds were successfully embedded in Pluronic-silica nanoparticles (PluS NPs), coupling the AIEgenic properties of these compounds with the exceptional colloidal stability and functional surface of this type of nanostructure.

Introduction

Nowadays, organic luminescent materials (OLM) that are highly bright in the solid state may have great potential for application in optoelectronic technologies and responsive and smart materials. Due to their interesting properties, trivalent and tetravalent organoboron compounds have become an important class of OLM.[1] Although known for decades, whereby many of them have been prepared and characterized, boron-containing luminescent polymers,[1f,2] such as tetra-coordinated boron complexes, remain valuable targets for material chemistry due to their good emissive, AIE, CIE, and MFC properties.[1f,2] They are thus the subjects for various structural modifications. The potential of tetra-coordinated boron compounds for the design of TADF emitters with high external quantum efficiency (EQE) has also been proved.[1a,b,d] Recently, boron-thioketonates were

prepared and characterized[3a] and some tetra-coordinated spiroborates (SBOX) were used as the host materials for blue OLEDs.[3b] Both NBN and – more recently – OBN heterocycles were synthesized and proposed for use in optical data encryption,[3c] OLED,[2g] and stimuli-responsive materials.[3d] The advantages of tetra-coordinated boron compounds are their stability towards both oxygen and moisture, as well as the ease of their preparation. These compounds can also be easily chemically modified allowing their properties to be tuned up.

The chemistry of tetra-coordinated boron complexes is very diverse. They may contain various ring sizes and heteroatom combinations, making their classification complex. Probably the simplest and clearest classification is the one based on the denticity of the ligand to which the boron atom is complexed, published by Tanaka *et al.*[1f] They divided the tetra-coordinated boron complexes into two large groups: with bidentate and tridentate ligands. Some representative general structures are shown in Chart 1.

A deep understanding of the structural properties and their relationships in OLMs is essential for tuning the characteristics of OLED devices in which they are used. Therefore, the synthesis and characterization of novel materials is an important and timely task for material organic chemistry.

In this work, we describe the synthesis, as well as the spectral, luminescence, and electrochemical properties of novel bicyclic and tricyclic tetra-coordinated NBN and OBN heterocycles **1** and **2** (see Chart 1). These compounds are important to realise our interest in the synthesis and characterization of polynitrogen

[a] *Institute of Organic Chemistry and Technology, University of Pardubice, Faculty of Chemical Technology, Studentská 573, CZ 532 10, Pardubice, Czech Republic. E-mail: marketa.svobodova@upce.cz, petr.simunek@upce.cz*

[b] *Dipartimento di Chimica ''Giacomo Ciamician'', Università di Bologna, via Selmi 2, 40126, Bologna, Italy*

[c] *Department of Analytical Chemistry, University of Pardubice, Faculty of Chemical Technology, Studentská 573, CZ 532 10, Pardubice, Czech Republic*

[d] *Department of General and Inorganic Chemistry, University of Pardubice, Faculty of Chemical Technology, Studentská 573, CZ 532 10, Pardubice, Czech Republic*
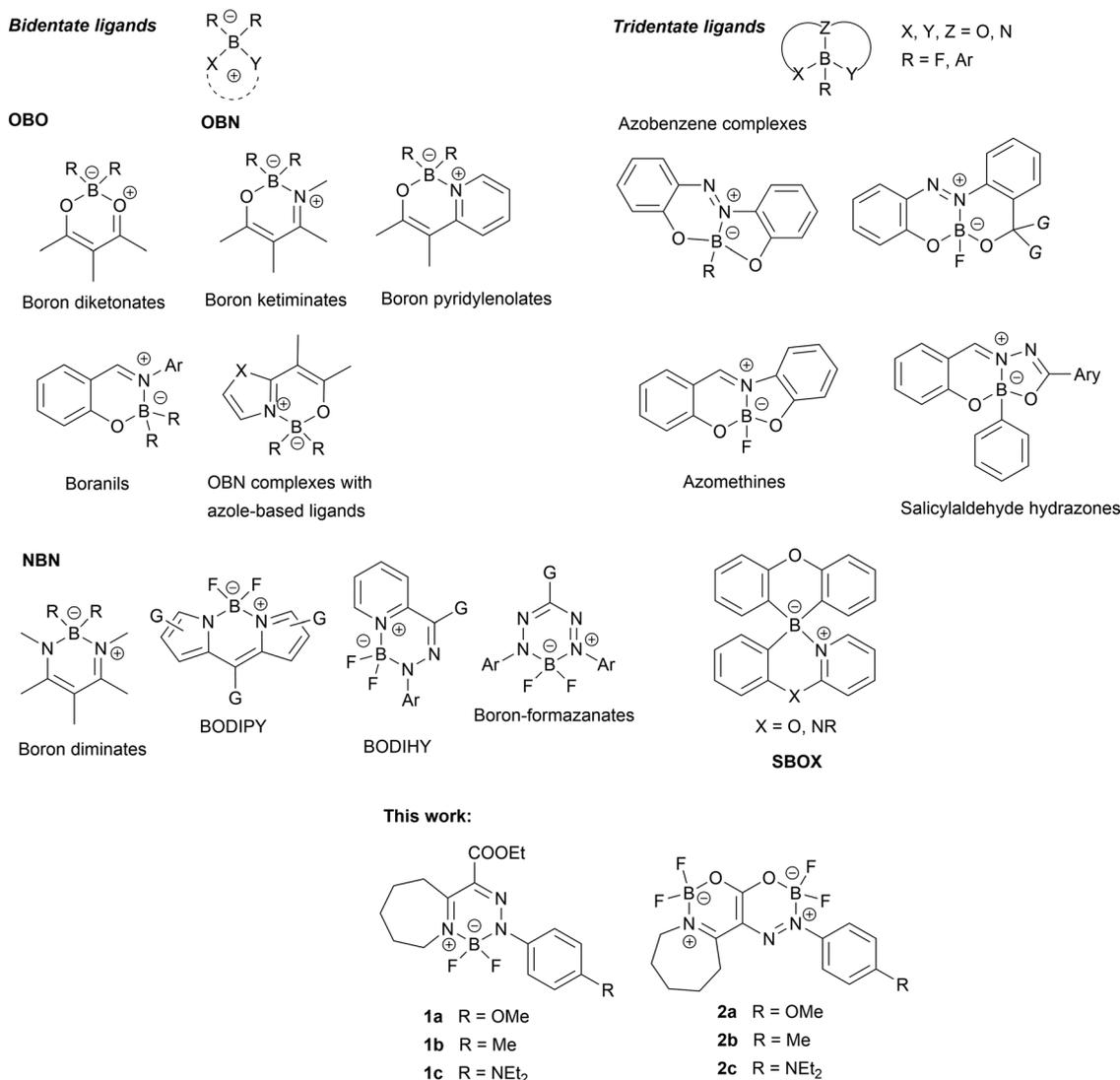
Tetra-coordinated boron complexes

Chart 1 Bidentate tetra-coordinated boron complexes and compounds studied in this work.

boron-containing heterocycles.[4] Seven-membered rings are incorporated in their structures, giving them the potential for RIV (restricted intramolecular vibration), and hence, making them AIEgens.[5a] This medium-ring strategy has been recently used to suppress aggregation-caused quenching (ACQ) at boron-based MR emitters.[5b] The presence of target functional groups allows us to unravel the relationships between the structure and physical properties of these NBN and OBN heterocycles, particularly highlighting the role of electron-donating substituents and the acid–base active pendants on the optical properties of these novel compounds.

Results and discussion

The target compounds were prepared according to Scheme S1. For experimental details and synthetic procedures see ESI.† The

suggested mechanism for the synthesis of **1** and **2** is depicted in Scheme S2 (ESI†).

NMR spectroscopy

Boron-11 and fluorine-19 NMR spectroscopy are useful tools for the structural study of BF$_2$-containing compounds. Both boron and fluorine NMR parameters sensitively reflect the electronic and steric surroundings.[6] Fluorine-19 NMR spectra of compound **1** consist of one 1:1:1:1 quartet due to the coupling with a single boron-11 nucleus ($I = 3/2$). It reveals that both the fluorine atoms are symmetrically equivalent. The equivalence could be due to either the planarity of the chelate ring or the exchange-average structure due to phenomena, such as fast ring-flipping. Therefore, the boron-11 signal is a simple triplet.

The analysis of boron-11 NMR spectra of compound **2** reveals a couple of triplets, indicating the presence of two different BF$_2$ fragments. Both the fluorine atoms within each

fragment are equivalent, probably due to fast ring-flipping. Therefore, the fluorine-19 spectra consist of two broad signals, one for each BF_2 fragment. In contrast to **1**, fine splitting is not observable here, probably due to the molecular dynamics leading to line-broadening. All the NMR spectra are deployed in ESI.†

Electrochemistry

Voltammetric techniques (cyclic voltammetry, rotating disk voltammetry) were employed to study the electrochemical properties of selected boron heterocycles in acetonitrile containing 0.1 M Bu_4N^+ PF_6^-. The electrochemical data are summarized in Table 1. Furthermore, representative cyclic voltammograms can be found in the ESI† (Fig. S64–S69, ESI†). The first oxidation of all the studied compounds proceeded at potentials from +1.81 to +0.66 V (*vs.* SCE) as a one-electron (quasi)reversible process (cathodic-anodic peak separation from 78 to 130 mV). The only exception was compound **2b**, where the (quasi)reversibility was observed at a higher scan rate (500 mV s^{-1}). Changes in the substitution significantly affected the oxidation of the boron heterocycle. In comparison of **1b** with **2b** and **1a** with **2a**, the addition of another borinine ring (*i.e.*, another electron acceptor) into the molecule caused the shift of the first oxidation potential by about 250 mV to more positive values. The same shift, but in the opposite direction (*i.e.*, towards less positive values), can be observed upon changing methyl (with +I effect) to a stronger electron-donating methoxy or diethylamino group. Furthermore, the first reduction of **1** and **2** proceeds at potentials from −0.86 to −1.42 V (*vs.* SCE) as the one-electron reversible process by the formation of a stable radical anion. Concerning different substitutions on the borinine core, the addition of another borinine ring (another redox center) extends the acceptor moiety. When comparing compound **1b** with **2b** (or **1a** with **2a**), the shift in the first reduction potential by approximately 440 mV to less negative values can be observed. On the other hand, the change in the electron-donating group within the series has a negligible effect on the first reduction potential (shift by about 50 mV). Moreover, the reduction in the second borinine ring can be found at ca −2 V. Last but not least, the difference between the first oxidation and reduction potential (see Table 1) reflects the delocalization of electron density in the molecule and is also aligned with the HOMO–LUMO gap (see Table 1).

Electronic spectra and theoretical studies

Electronic spectra of compound **1** measured in acetonitrile (Fig. 1) consist of one broad band across 389–472 nm. The wavelength of the band correlates with the electronic properties
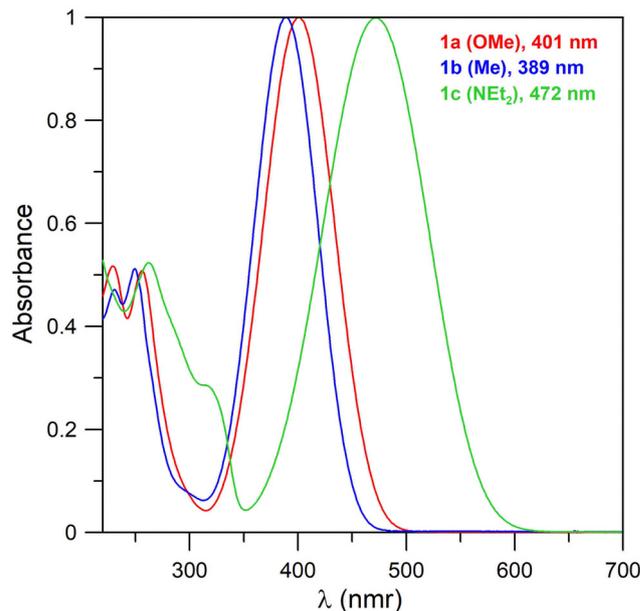

Fig. 1 Normalized UV-vis spectra of triazaborines **1a–c** in acetonitrile.

of the substituents and increases in the order Me < OMe < NEt$_2$. The intensity of the band is comparable for all the compounds with ε of approximately 10 000. These bands correspond to the π–π* transitions. The less intense bands containing multiple peaks with maxima of ~250 nm correspond to benzenoid bands (B bands).

UV-vis spectra of bis-boron derivatives **2** (Fig. 2) also consist of broad bands across 389–517 nm, corresponding to the π–π* transitions. The value for methyl derivative **2a** (389 nm) is the same as for its **1a** analogue. The maxima of the bands for the other two compounds are shifted bathochromically in comparison with their mono-boron analogues (401 → 409 nm for the OMe derivative and 472 → 517 nm for the NEt$_2$ derivative). The order of the maxima also corresponds with the electronic properties of the substituents. The absorption properties thus appear to be more strongly dependent on the nature of the substituents rather than on the mono- or bis-boron heterocyclic structure. This also illustrates the localisation of HOMO orbitals (Fig. 3).

Wavelengths of the main absorption bands, together with their absorption coefficients, for compounds **1** and **2** are summarized in Table 1.

For a deeper insight into the absorption properties, the TD-DFT calculations (B3LYP-6311+G(d,p)) were performed with acetonitrile as the solvent (CPCM). For the simplification of

Table 1 Electronic properties of compounds **1** and **2**

| Compound	λ_{max} (nm)	ε (dm^{-3} cm^{-1} mol^{-1})	$\lambda_{A(max)}$ calc (nm)	f	Transition	Main orbital transition	E^{oF} (ox1) (V) *vs.* SCE	E^{oF} (red1) (V) *vs.* SCE	$E_{ox1}^{oF}-$ E_{red1}^{oF} (V)	HOMO–LUMO gap (eV)
1a	401	9577	412	0.54	$S_0 \rightarrow S_1$	HOMO→LUMO	1.32	−1.34	2.66	3.44
1b	389	10 023	386	0.57	$S_0 \rightarrow S_1$	HOMO→LUMO	1.56	−1.29	2.85	3.66
1c	472	9499	495	0.57	$S_0 \rightarrow S_1$	HOMO→LUMO	0.66	−1.42	2.08	2.86
2a	409	24 813	398	0.69	$S_0 \rightarrow S_1$	HOMO→LUMO	1.56	−0.90	2.46	3.25
2b	389	24 890	432	0.69	$S_0 \rightarrow S_1$	HOMO→LUMO	1.81	−0.86	2.67	3.53
2c	517	13 449	521	0.76	$S_0 \rightarrow S_1$	HOMO→LUMO	0.84	−1.00	1.84	2.63

Paper — **Materials Advances**
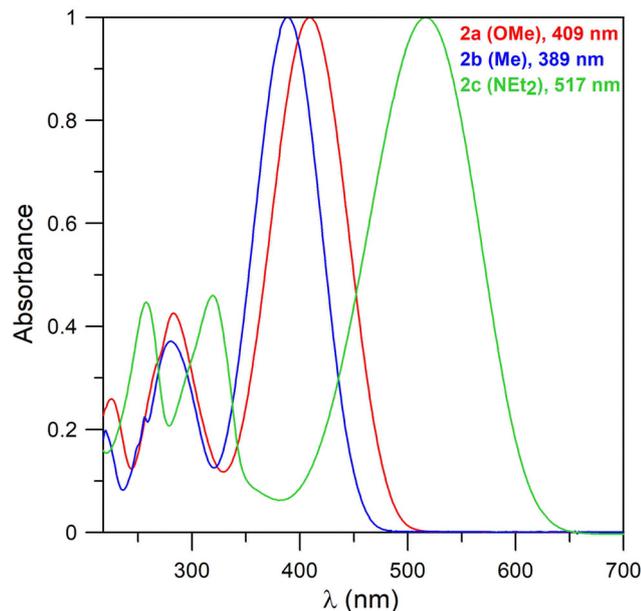
Fig. 2 Normalized UV-vis spectra of compounds **2a–c** in acetonitrile.

the calculations, the ethyl groups were substituted by methyl groups. The energy levels of HOMO−1, HOMO, LUMO, and LUMO+1 together with the orbital locations are depicted in Fig. 3. Results of the calculations are summarized in Table 1 to show that the red emission of both NEt$_2$ derivatives is largely due to the increase in the energy of the HOMO, resulting in strong destabilization by the charged character introduced by the nitrogen atom.

Luminescence and AIE properties

The emission of diluted solutions of compounds **1a**, **1b**, **2a**, and **2b** in acetonitrile (concentration 5 μM) was very low, with PLQY below 0.01, as desired for high contrast luminogenic properties in AIE compounds. The emission spectra of the same compounds in the solid state (powder) measured with an integrating sphere, revealed intense yellow-orange photoluminescence upon excitation at λ_{exc} = 400 nm, with broad non-structured emission bands peaking at 560 nm (compounds **1a** and **2a**) or 525 nm (compounds **1b** and **2b**). Photoluminescence quantum yield (PLQY) was estimated to be in the range 0.18–0.5 for the four compounds (see Table 2 and Fig. 4). In addition, compound **1c** showed a good enhancement of PLQY in the solid state compared to diluted acetonitrile solution (from 0.017 to 0.15), while compound **2c** has only a low and constant PLQY
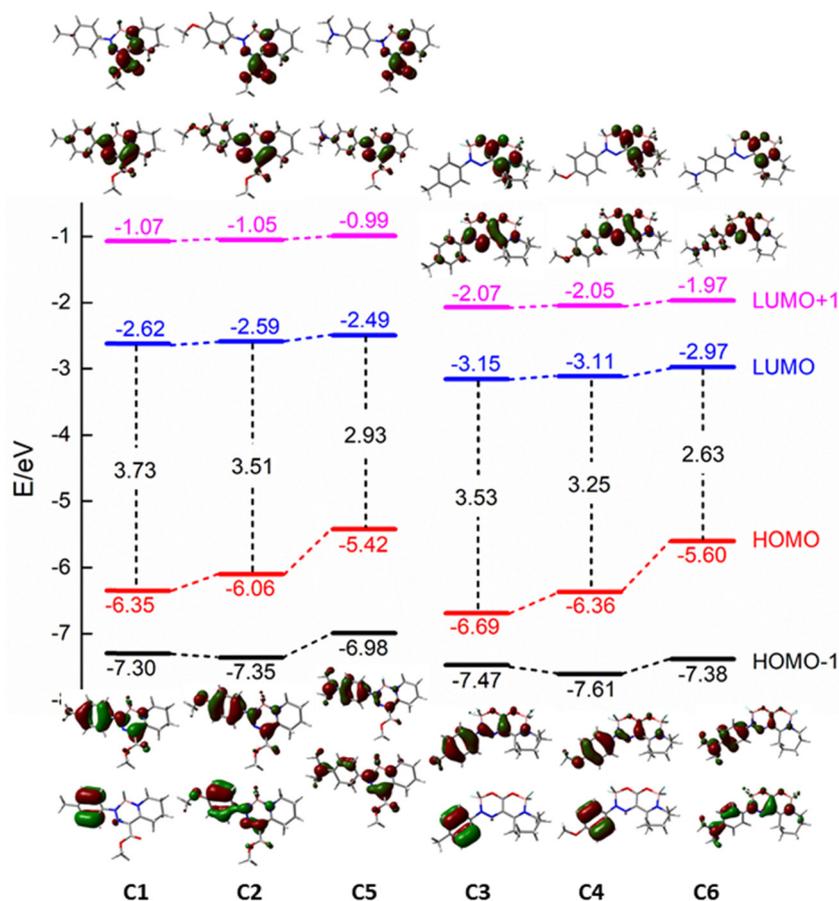

Fig. 3 Molecular orbital energy diagram and iso-density surface (contour value 0.04) plots of the HOMO−1, HOMO, LUMO, and LUMO+1 orbitals calculated at the B3LYP/6-311+G(d,p) level of theory in CH$_3$CN.

Table 2 Photophysical properties (photoluminescence quantum yield, emission lifetime, and peak wavelength) of compounds **1** and **2**

Compound	solid state			Aggregate		
	PLQY	τ (ns)	$\lambda_{em.max}$ (nm)	PLQY	τ (ns)	$\lambda_{em.max}$ (nm)
1a	0.13	1.70	568	0.15	1.98	560
1b	0.51	3.33	521	0.27	3.08	526
1c	0.15	1.84	620	0.10	0.19[a]	625
2a	0.18	2.62	568	0.22	1.89[a]	560
2b	0.47	2.72	527	0.31	1.85[a]	521
2c	0.014	0.71[a]	716	0.002	0.33[a]	645

[a] Average lifetime (by intensity) of a multiexponential decay.

($\sim$0.02) at both conditions. Interestingly, compound **1c** is a bright solid-state emitter in the red spectral region. Compound **2c** shows a narrow and bathochromically shifted emission band in the solid state (compared to the solution, Fig. S58, ESI†), which may suggest the onset of J-aggregates for this compound. On the contrary, all other compounds in the solid state show emissions in the same wavelength range as in diluted acetonitrile solution.

Triggered by this observation, we investigated the aggregation-induced emission (AIE) of these compounds by preparing solutions in acetonitrile/water mixtures with increasing water content. Formation of emissive aggregates was observed for all compounds except **2c**, at a water content of at least 80% v/v (Fig. 5). In acetonitrile, the solutions are stable with no sign of aggregation even in the millimolar range. In water, instead, aggregates are formed readily even at the lowest concentration of 5 µM with clear AIE. Compound **1a** only forms aggregates at a concentration of at least 20 µM in water with a peculiar kinetic activation (Fig. S61, ESI†). These aggregates are roughly as emissive as the solid powder with a similar lifetime for **1a** and **1b** and a shorter and multiexponential lifetime in the case of **1c**, **2a**, and **2b** (Table 2). The multiexponential lifetime is ascribable to a distribution of the dyes (see below

Fig. 4 Normalized emission spectra of compounds **1a**, **b**, **c** and **2a**, **b**, **c** in the solid state (λ_{exc} = 400 nm).

FLIM results). The aggregates also feature different colloidal stability: **2a** and **2b** form rather stable aggregates in water (Fig. 5D), while **1a** and **1b** have a clear tendency to sediment and stick at interfaces (microscopy images in Fig. S63, ESI†). Compounds **1c** and **2c** are soluble in acidic water due to the protonation of the tertiary amine, which results in blue-shifted absorption and emission (see Fig. S57 and S58 in ESI†). The non-protonated species, on the contrary, are much less water-soluble and form aggregates, while **1c** shows a large enhancement in its luminescence upon deprotonation (>10 fold) due to the onset of AIE triggered by the lower solubility of the non-charged species. On the contrary, **2c** does not show a significant increase in its brightness upon deprotonation and forms aggregates. For instance, in the solid state, its quantum yield remains very low. It is noteworthy that the acid–base nature of compound **1c** makes it a good candidate for application as a pH-responsive AIE luminogen.

Finally, we measured the emission decay after deoxygenation (purged with N_2) to reduce the quenching of the triplet and to observe eventual TADF. Yet, significantly delayed emissions were not observed for long lifetime components, even upon removal of oxygen, neither in the solid state nor in the aggregates in water.

The aggregates formed in water were further analysed with confocal microscopy and fluorescence lifetime imaging (FLIM). Aggregates of compounds **1a** and **1b**, which were the most unstable in water, were difficult to find and could only be observed in large masses of aggregates at the boundary of the water droplet. In contrast, the aggregates of compounds **2a** and **2b** were distributed in the water droplet and on the surface of the cover glass. In particular, the aggregates of **2b** were homogeneous in size (Fig. 5). Interestingly, FLIM images confirm that the emission decay of these aggregates is shorter than the emission in the solid state and multiexponential. Furthermore, FLIM of **2b** reveals that aggregates, despite being homogeneous in size, are surprisingly polydisperse in terms of their emission lifetime, suggesting that during the formation of the aggregate, the dyes can assume different conformations with slightly different photophysical properties.

The reproducibility and long-term stability of these water-dispersed aggregates are unsolved issues and limit the application potential of their luminescence. To enhance the colloidal and photophysical stability of the AIE aggregates in water, we attempted to physically entrap the compounds as small, monodisperse, and water-soluble nanoparticles (NPs), composed of a silica core and PEG shell.[7] The synthesis of these nanoparticles is based on a well-established procedure[7] using tetraethoxysilane (TEOS) as the monomeric precursor and Pluronic F127 micelles as the template, which yields homogeneous particles of typical core and shell diameters of 10 and 25 nm, respectively.

We prepared NPs with encapsulated AIE-active compounds **1a**, **1b**, **2a**, and **2b** at relatively low degrees of doping (0.05% mol mol^{-1} TEOS) to minimize their interference with the formation of nanoparticles. Compounds **1c** and **2c** were not included owing to their water solubility in an acidic environment, which hinders the entrapment in hydrophobic micelles, and thus, in NPs. A clear peak was observed at $\sim$25 nm with DLS
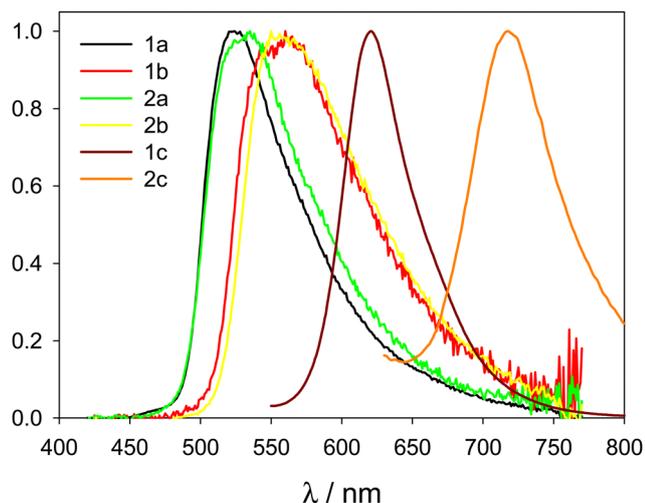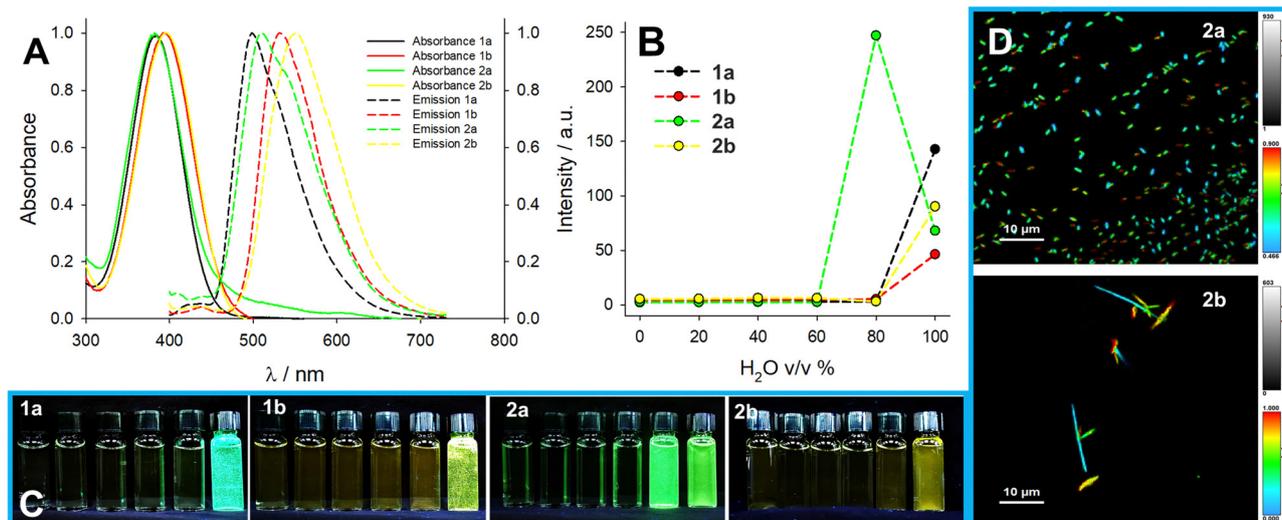
Fig. 5 AIE properties: (A) Normalized absorbance and emission spectra of compounds **1a**, **1b**, **2a**, and **2b** in water (20 µM) and (B) trends of emission intensity at peak (λ_{exc} = 360 nm) in acetonitrile:water mixtures at increasing water content (full absorbance and emission spectra in Fig. S59 and S60, ESI†). (C) The photographs under UV light of compounds **1a**, **1b**, **2a**, and **2b** in acetonitrile:water mixtures at increasing water content. (D) FLIM images of samples **2a** and **2b** in water.

measurements for all prepared NPs; this is expected for this kind of NPs, but compounds **2a** and **2b** resulted in an additional peak at a very large diameter, probably due to the formation of dye aggregates independently from the formation of NPs, resulting in large average diameter and polydispersity index (PdI, see Table 3). Nonetheless, the DLS of NPs prepared in the presence of compounds **1a** and **1b** revealed the presence of a peak at ~25 nm, suggesting a successful formation of dye-doped NPs.

The absorbance spectra of the prepared nanoparticles (Fig. 6) with AIE dyes embedded in them confirm the presence of large scattering aggregates for **2b@NPs**, while the band of **2a@NPs** is not present because of the precipitation of the aggregates before the measurement, also confirming that **2a** was not efficiently incorporated in the NPs.

On the contrary, compounds **1a** and **1b** are efficiently incorporated in the nanoparticles: scattering of the solutions is low as expected for these small NPs, and the absorbance peaks confirm the presence of dyes **1a** and **1b**. From the
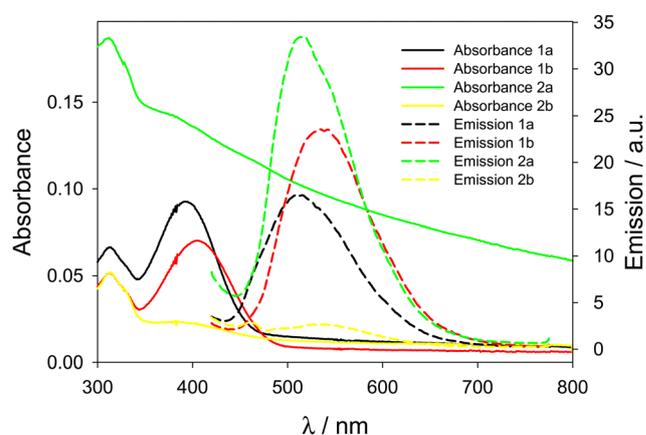

Fig. 6 Absorbance (solid lines) and emission spectra (dashed lines, λ_{exc} = 400 nm and cut-off filter at 435 nm) of NPs embedding compounds **1a**, **1b**, **2a**, and **2b**.

absorbance spectra, from the known molar extinction coefficient of the dyes and the concentration of NPs (known and reproducible for this preparation method[7]), we calculated the effective doping degree of the dyes in the nanoparticles, confirming an efficient encapsulation of these two dyes (Table 3). Finally, the PLQY of **1a@NPs** and **1b@NPs** is lower compared to the aggregates in water, suggesting non-optimal AIE properties in this type of NPs, possibly due to residual molecular mobility. The analysis of the emission decays reveals short and multi-exponential lifetimes for **1a@NPs** and **1b@NPs** in NPs, further corroborating this hypothesis (Table 3).

Crystallography

As for the crystallographic properties of these compounds, both complexes **1a** and **2a** crystallize in the monoclinic space group ($P2_1/c$) with four molecules in the crystal lattice. All the core

Table 3 Properties of NPs

NPs	ϕ_{av} (nm), PdI[a]	% Doping[b]	PLQY	τ (ns)	B	χ^2	τ_{av}[c] (ns)
1a	22.4; 0.140	0.046	0.070	0.41	23 100	0.868	0.71
				1.29	10 500		
				4.90	240		
1b	30.2; 0.229	0.048	0.040	0.30	25 200	0.922	0.51
				1.15	7100		
				5.22	170		
2a	289; 0.343						
2b	483; 0.630						

[a] Obtained from DLS. [b] Obtained from absorbance spectra. [c] The average lifetimes (τ_{AV}) are calculated on the values of the pre-exponential coefficient B.
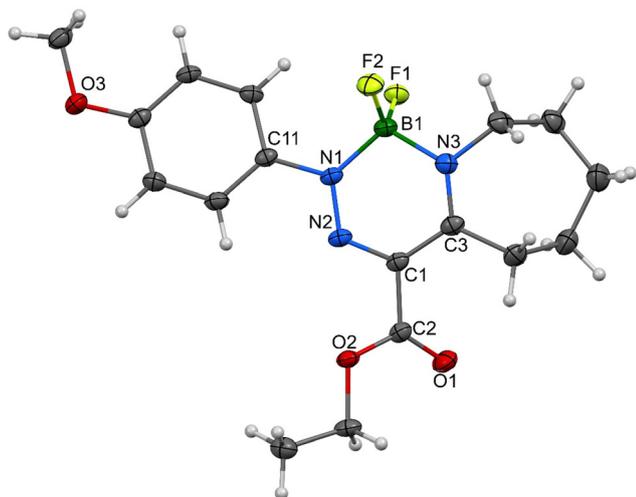
Fig. 7 Molecular structure of **1a**, ORTEP view, 50% probability level; selected interatomic distances [Å] and bond angles [°] are given in Table S5 (ESI†).

six-membered rings, which contain four and three heteroatoms, respectively, are essentially planar with highly conjugated systems of π-electrons. In addition, the 4-methoxyphenyl substituents in **1a** are nearly coplanar with that system and only slightly deviated (27.5°) in **2a**. Propylene parts of the tetrahydroazepine substituent located opposite the C=N connectors are screwed out of the central plane of both molecules. The interatomic distances and angles around the boron atoms (see Fig. 7–10) are in line with previously found values for single bonds. On the other hand, the azenyl parts of the molecules exhibit bigger differences when compared mutually and to the values found for N=N bonds too. In **1a**, the conjugation of the six-membered system causes the elongation of this bond up to 1.3128 (16) Å, but the same type of bond is much shorter for N1–N2, *i.e.*, 1.2882 (15) Å, in **2a**. In the same complex, the arrangement within the carboxylate unit bridging two borate anions (C2–C1(–O1)–O2) exhibits extremely short distances between involved atoms. Such a system, which is presumably described as a geminal diolate with a double bond between the C2 and C1 atoms has nearly equidistant C–O separations that
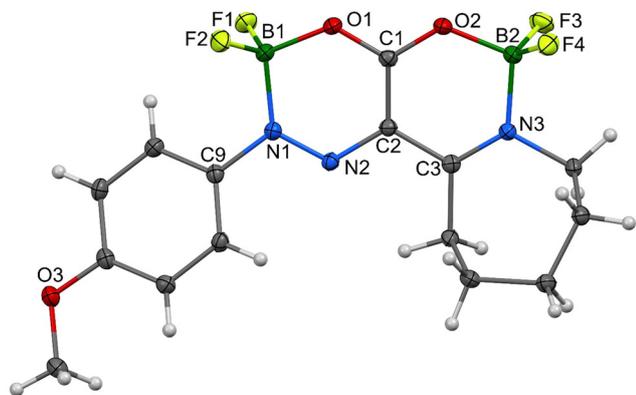

Fig. 8 Molecular structure of **2a**, ORTEP view, 50% probability level; selected interatomic distances [Å] and bond angles [°] are given in Table S6 (ESI†).
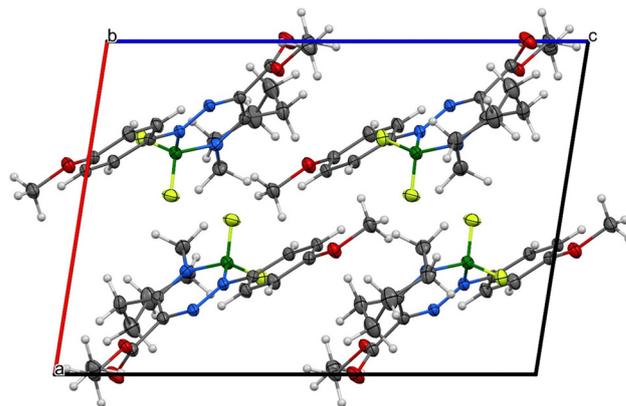

Fig. 9 Supramolecular architecture/crystal packing of **1a**, view along the *b*-axis.
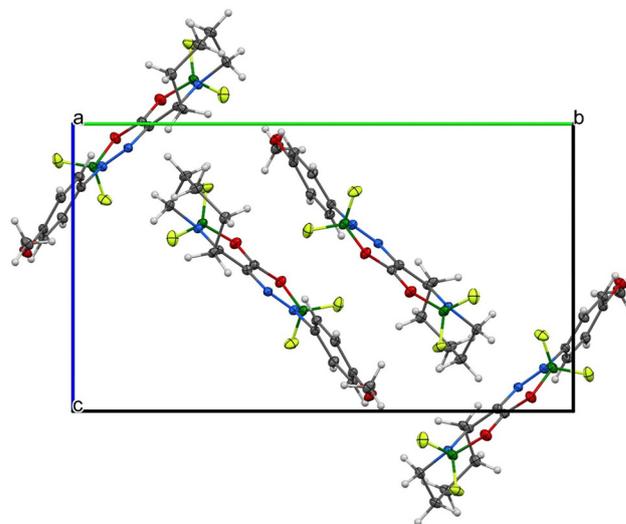

Fig. 10 Supramolecular architecture/crystal packing of **2a**, viewed along the *a*-axis.

are smaller than 1.28 Å, and thus, are more likely approaching an extreme situation in isobidentate carboxylates. Similar distances were found only in structures with a complex ionic-zwitterionic structure containing tetramethyl and trimethyl-phosphonium moieties or bridging carboxylate groups.[7,8]

Due to the presence of the non-planar tetrahydroazepine substituent, both complexes cannot adopt π–π stacking, and only corrugated layers of centrosymmetrically related molecule pairs are found. Efforts of molecules to planarize in the solid state are more pronounced in **1a** than in **2a** (see Fig. 7–10). For experimental details, see Tables S3 and S4 (ESI†). For bond lengths and angles, see Tables S5 and S6 (ESI†).

Conclusions

Six novel difluoroboron heterocycles having either N–B–N or O–B–N arrangements were prepared and characterized using electrochemical and spectral (NMR, UV-vis, luminescence)

methods. For two cases analysed here, X-ray diffraction analysis was also successfully performed. The results obtained were corroborated by DFT calculations.

Except for **2c**, all the prepared compounds show negligible luminescence in acetonitrile solutions and turn intensely luminescent in the solid state. Compounds **1a, b** and **2a, b** present a bright yellow-orange luminescence, whereas the luminescence of **1c** is red. Therefore, the functionalization with ethers or tertiary amines is a good strategy for tuning the emissive properties of NBN and OBN compounds. These compounds are AIE active in a dioxan–water mixture.

Encapsulating **1a** and **1b** dyes in silica-PEG nanoparticles can represent an effective way to stabilize AIE aggregates and obtain increased emission in comparison with the solution phase, despite the PLQY enhancement being limited by residual mobility in this kind of NP. The average lifetimes are similar to the ones obtained for aggregates in water and lower than the ones measured for the solid state (0.51–0.74 ns).

Overall, the functionalization of mono-boron heterocycles containing the NEt_2 group has proven to be a promising strategy to introduce pH responsiveness in this class of AIE-active compounds: AIE can be activated or the emissive aggregate disrupted upon deprotonation and protonation, respectively.

Experimental

Synthetic procedures, instrument details, as well as other characterization data are included in the ESI.†

Data availability

All the data supporting the conclusions made in this manuscript are a part of the ESI.†

Conflicts of interest

There are no conflicts to declare.

References

1 (a) S. S. Kothavale and J. Y. Lee, Adv. Opt. Mater., 2020, 2000922; (b) H. Lee, D. Karthik, R. Lampande, J. H. Ryu and J. H. Kwon, Front. Chem., 2020, 8, 373; (c) M. Hayakawa, M. Kameda, R. Kawasumi, S. Nakatsuka, N. Yasuda and T. Hatakeyama, Angew. Chem., Int. Ed., 2023, e202217512; (d) G. Li, W. Lou, D. Wang, C. Deng and Q. Zhang, ACS Appl. Mater. Interfaces, 2019, 11, 32209; (e) A. Chandrasekar Murali, P. Nayak, S. Nayak, S. Das, S. P. Senanayak and K. Venkatasubbaiah, Angew. Chem., Int. Ed., 2023, e202216871; (f) K. Tanaka, M. Gon, S. Ito, J. Ochi and Y. Chujo, Coord. Chem. Rev., 2022, 472, 214779.

2 (a) Y.-L. Rao and S. Wang, Inorg. Chem., 2011, 50, 12263; (b) D. Li, H. Zhang and Y. Wang, Chem. Soc. Rev., 2013, 42, 8416; (c) D. Frath, J. Massue, G. Ulrich and R. Ziessel, Angew. Chem., Int. Ed., 2014, 53, 2290; (d) S. S. Kothavale and J. Y. Lee, Adv. Opt. Mater., 2020, 2000922; (e) H. Lee, D. Karthik, R. Lampande, J. H. Ryu and J. H. Kwon, Front. Chem., 2020, 8, 373; (f) S. K. Mellerup and S. Wang, Chem. Soc. Rev., 2019, 48, 3537; (g) S. Mukherjee and P. Thilagar, J. Mater. Chem. C, 2016, 4, 2647.

3 (a) A. Chandrasekar Murali, P. Nayak, S. Nayak, S. Das, S. P. Senanayak and K. Venkatasubbaiah, Angew. Chem., Int. Ed., 2023, e202216871; (b) M. Hayakawa, M. Kameda, R. Kawasumi, S. Nakatsuka, N. Yasuda and T. Hatakeyama, Angew. Chem., Int. Ed., 2023, e202217512; (c) X. Zhu, R. Liu, Y. Li, H. Huang, Q. Wang, D. Wang, X. Zhu, S. Liu and H. Zhu, Chem. Commun., 2014, 50, 12951; (d) G. Tan, I. Maisuls, F. Strieth-Kalthoff, X. Zhang, C. Daniliuc, C. A. Strassert and F. Glorius, Adv. Sci., 2021, 8, 2101814.

4 (a) M. Svobodová, J. Bárta, P. Šimůnek, V. Bertolasi and V. Macháček, J. Organomet. Chem., 2009, 694, 63; (b) F. Josefík, M. Svobodová, V. Bertolasi, P. Šimůnek, V. Macháček, N. Almonasy and E. Černošková, J. Organomet. Chem., 2012, 699, 75; (c) M. Svobodová, P. Šimůnek, V. Macháček, L. Štruncová and A. Růžička, Tetrahedron, 2012, 68, 2052; (d) F. Josefík, T. Mikysek, M. Svobodová, P. Šimůnek, H. Kvapilová and J. Ludvík, Organometallics, 2014, 33, 4931.

5 (a) J. Mei, N. L. C. Leung, R. T. K. Kwok, J. W. Y. Lam and B. Z. Tang, Chem. Rev., 2015, 115, 11718; (b) B. Lei, Z. Huang, S. Li, J. Liu, Z. Bin and J. You, Angew. Chem., Int. Ed., 2023, e202218405.

6 (a) F. P. Macedo, C. Gwengo, S. V. Lindeman, M. D. Smith and J. R. Gardinier, Eur. J. Inorg. Chem., 2008, 3200–3211; (b) H. Doušová, P. Šimůnek, N. Almonasy and Z. Růžičková, J. Organomet. Chem., 2016, 802, 60; (c) H. Doušová, N. Almonasy, T. Mikysek, J. Váňa, M. Nepraš, B. Frumarová, M. Dvořák, Z. Růžičková and P. Šimůnek, Monatsh. Chem., 2018, 149, 1975.

7 (a) F. Palomba, D. Genovese, L. Petrizza, E. Rampazzo, N. Zaccheroni and L. Prodi, Sci. Rep., 2018, 17095; (b) D. Genovese, M. Montalti, L. Prodi, E. Rampazzo, N. Zaccheroni, O. Tosic, A. Altenhöner, F. May and J. Mattay, Chem. Commun., 2011, 47, 10975; (c) D. Genovese, E. Rampazzo, N. Zaccheroni, M. Montalti and L. Prodi, Eur. J. Inorg. Chem., 2017, 5094; (d) E. Rampazzo, S. Bonacchi, D. Genovese, R. Juris, M. Montalti, V. Paterlini, N. Zaccheroni, C. Dumas-Verdes, G. Clavier, R. Méallet-Renault and L. Prodi, J. Phys. Chem. C, 2014, 118, 9261.

8 (a) M. Radius, E. Sattler, H. Berberich and F. Breher, Chem. – Eur. J., 2019, 25, 12206; (b) H. Binder, W. Matheis, H.-J. Doiseroth and H. Fu-Son, Z. Naturforsch., B: J. Chem. Sci., 1983, 38, 554; (c) H. Binder, W. Matheis, H.-J. Deiseroth and H. Fu-Son, Z. Naturforsch., B: J. Chem. Sci., 1984, 39, 1717; (d) H. Binder, W. Matheis, G. Heckmann, H.-J. Deiseroth and H. Fu-Son, Z. Naturforsch., B: J. Chem. Sci., 1985, 40, 934.